ARTICLE

Check for updates

Coupled mechanical oscillator enables precise detection of nanowire flexural vibrations

Maneesha Sharma[1✉], Aniruddha Sathyadharma Prasad [1], Norbert H. Freitag [1], Bernd Büchner [1,2] & Thomas Mühl [1✉]

The field of nanowire (NW) technology represents an exciting and steadily growing research area with applications in ultra-sensitive mass and force sensing. Existing detection methods for NW deflection and oscillation include optical and field emission approaches. However, they are challenging for detecting small diameter NWs because of the heating produced by the laser beam and the impact of the high electric field. Alternatively, the deflection of a NW can be detected indirectly by co-resonantly coupling the NW to a cantilever and measuring it using a scanning probe microscope. Here, we prove experimentally that co-resonantly coupled devices are sensitive to small force derivatives similar to standalone NWs. We detect force derivatives as small as 10^{-9} N/m with a bandwidth of 1 Hz at room temperature. Furthermore, the measured hybrid vibration modes show clear signatures of avoided crossing. The detection technique presented in this work verifies a major step in boosting NW-based force and mass sensing.

[1] Leibniz Institute for Solid State and Materials Research IFW Dresden, 01069 Dresden, Germany. [2] Institute of Solid State and Materials Physics, Technische Universität Dresden, 01069 Dresden, Germany. ✉email: m.sharma@ifw-dresden.de; t.muehl@ifw-dresden.de

In the last two decades, new ways of growing pristine nanoscopic wires have been developed enabling fields of research that facilitate the development of entirely new generations of sensors and electronic devices to unveil the physics at the nanoscale. Nanowires (NWs) have entered the research fields of electronics[1], biosensors[2], energy harvesting and storage[3], drug delivery[4], wearable devices[5–7], environmental applications[8], optical spectroscopy with nanometer resolution[9], mass sensing[10,11], and force sensing[12–16]. In addition, advancements in nanoscale characterization techniques have made it much easier to harness the potential of NWs.

For NW-based mass and force sensing, device geometries that support flexural vibrations of the NW are used where vibration properties such as eigenfrequencies or amplitudes respond to small interaction forces or attached masses. Singly-clamped NWs can be considered as miniaturized cantilever force transducers with a large dynamic range of linear operation[17]. The minimal measurable force of such NWs as limited by its thermal noise is given by $F_{\min} = \sqrt{4k_{\mathrm{B}}TB\Gamma}$ with k_{B} referring to the Boltzmann constant, T the temperature, B the measurement bandwidth and Γ the mechanical dissipation constant. Based on $\Gamma = \omega_0 m_{\mathrm{eff}}/Q$, where ω_0 is the resonance frequency, m_{eff} the effective mass of the resonator, and Q the mechanical quality factor, it can be shown that $F_{\min} \propto d/\sqrt{l}$ where d is the NW diameter and l its length[13]. Hence, highly sensitive force measurements require thin and long cantilevers, requirements that are naturally satisfied by high aspect ratio NWs. In the case of NW-based devices for torque measurements, including approaches for nanomagnetometry[18,19], the sensitivity is limited by the minimum detectable torque given by $\tau_{\min} = l_{\mathrm{eff}}F_{\min} \propto d\sqrt{l_{\mathrm{eff}}}$ where l_{eff} is the effective length of the NW beam. Hence, for high-sensitivity torque measurements, a thin and short NW would be preferred. In general, further miniaturization of NWs' dimensions holds great potential for achieving unprecedented sensitivity.

Deflections and flexural oscillations of singly-clamped NWs can be detected by interferometry for NW diameters above 50 nm[20]. Below this diameter detection becomes challenging. Detection of vibrations in the case of thinner NWs can be accomplished by the attachment of an optical scatterer at the free NW end[21], by an NW interaction with a focused electron beam[11,22], or by exploitation of field emission patterns[23–25]. However, the latter requires a sophisticated image analysis technique to interpret the oscillating emission pattern.

An alternative is the detection of flexural vibrations of the NW by mechanically coupling them to easy-to-detect cantilevers (CLs) and by the exploitation of coupled or hybrid vibration modes[26–29]. This approach is also referred to as the co-resonant detection concept since it relies on matched individual eigenfrequencies of NW and cantilever, i.e., $\omega_{\mathrm{NW}} \approx \omega_{\mathrm{CL}}$ where fundamental or higher-order flexural modes can be used. Even when considering two simple harmonic oscillators with one oscillation mode each, coupling of them leads to two new hybrid oscillation modes with eigenfrequencies ω_{a} and ω_{b}. Such systems can be described as two degrees of freedom resonators[30]. In the case of matched individual eigenfrequencies, both coupled modes are detectable at the cantilever despite the huge size asymmetry $m_{\mathrm{CL}} \gg m_{\mathrm{NW}}$ of the subsystems where m_{CL} and m_{NW} are the masses of the cantilever and the NW, respectively[26].

The key advantages of the co-resonant approach include: (i) The sensors can be read out with any conventional cantilever deflection detection setup as used in commercial scanning probe microscopy (SPM) equipment. (ii) It is based on a design, where the NW vibration is detected by purely mechanical coupling to a cantilever. Therefore, direct optical detection of the NW vibrations and its limitations in the case of small NW diameters are avoided. For example, optical heating of NWs due to interactions with the laser beam can be ruled out. (iii) Compared to focused electron-beam detection techniques, an optically detected co-resonant sensor is not subjected to the risk of unwanted deposition of contaminants or any electrical charging issues.

Other published sensor concepts based on the coupling of two oscillators with similar eigenfrequencies but very different spring constants include the Akiyama SPM probe[31] consisting of a soft U-shaped cantilever coupled to a quartz tuning fork and stepped cantilevers[32] for improved mass sensing.

Previously, it has been demonstrated that co-resonantly coupled oscillation systems enable high-sensitivity magnetometry of ferromagnetic nanoparticles even when using a cantilever with a spring constant as high as $k_{\mathrm{CL}} = 1.4\,\mathrm{N/m}$ as part of the coupled system[28]. Nevertheless, until now there is no conclusive experimental proof that a co-resonant sensor can, by design, detect smaller interactions than the standalone cantilever.

In this work, we show experimentally that small force derivatives, that are not detectable at a particular cantilever due to fundamental thermodynamical reasons, lead to clearly observable frequency shifts when measuring vibration modes of a co-resonantly coupled system consisting of the same cantilever and a silicon nanowire. The measured force derivatives are of the order of $10^{-9}\,\mathrm{N/m}$.

Results and discussion

Fabrication and frequency matching of coupled devices. For our devices, we used silicon nanowires (Si NWs) and tip-less Si cantilevers (see "Fabrication of coupled oscillator devices" in the "Methods" section). We prepared and characterized two coupled oscillator devices (device #1 and device #2, Fig. 1a, b, Table 1, and Supplementary Note 1).

During the device fabrication process, we track the resonance frequencies of fundamental flexural vibration modes of both cantilever and NW by electron-beam-based mechanical motion detection[22]. Usually, two NW flexural resonances close to each other are detected that refer to orthogonal modes of vibration caused by slightly asymmetric NW cross-sections[33,34]. However, depending on the mode directions, their projections onto the SEM scanning plane may provide very different apparent amplitudes. Thus, we selected devices where the apparent amplitude of one of these orthogonal modes is at least 10 times larger than the other one. Since the cantilever is mounted on the SEM stage in such a way that its vibration direction is in the scanning plane, the observed dominant NW mode will be best suited to be coupled to the cantilever's fundamental flexural mode. We achieve co-resonant coupling of the NW oscillator with the cantilever by changing the eigenfrequency of the selected NW mode (i.e., $\omega_{\mathrm{NW}} \approx \omega_{\mathrm{CL}}$ with $\omega_i = \sqrt{k_i/m_i}$). The frequency matching is done by deposition of tungsten onto the free NW end (by electron-beam-assisted deposition and by attachment of small pieces of a tungsten nanomanipulator tip), which increases the NW's effective mass m_{NW} (see Fig. S1 of Supplementary Information).

Measurement of coupled vibration modes. The coupled cantilever sensor is mounted at a tilt angle of $10°$ in a conventional high-vacuum SPM setup (NanoScan AG hrMFM) with cantilever detection by a laser beam deflection system (Fig. 1a). To tailor the coupled modes, a DC bias voltage V can be applied between the coupled device and a parallelly aligned Si substrate located 1 mm below. To capture and process the cantilever deflection signal we use a lock-in amplifier (Zurich Instruments HF2LI). An example of measured thermal displacement noise power spectral density (PSD) is shown in Fig. S2 (see Supplementary Note 2). The
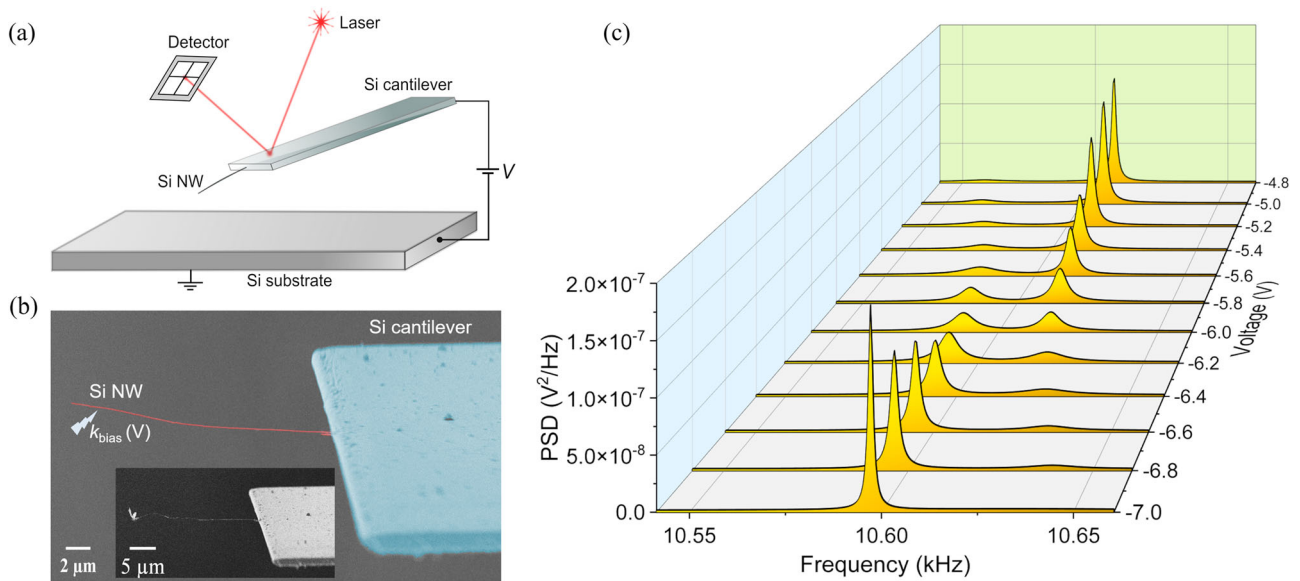
Fig. 1 Experimental setup and *V*-dependent frequency response. a Scheme of the detection technique where thermal fluctuations are read at the cantilever in a conventional scanning probe microscopy (SPM) device. **b** Scanning electron microscopy (SEM) image of a coupled oscillator consisting of a silicon nanowire (Si NW) and a tip-less Si cantilever (device #1). The lightning bolt symbol indicates a bias voltage-induced force derivative acting on the coupled oscillator as described by k_{bias}. Inset: The same coupled oscillator after frequency matching by electron-beam-assisted deposition onto the NW free end. **c** Waterfall plot of cumulative curve fitting of the *V*-dependent power spectral density (PSD) of the thermal noise measured optically at the cantilever of device #1 at room temperature.

Table 1 Properties of the Si cantilevers and nanowires.

		Device #1	Device #2
Cantilever	k_{CL} (N/m)	0.126	0.140
	m_{CL} (kg)	2.85×10^{-11}	3.18×10^{-11}
	$\omega_{CL}/2\pi$ (kHz)	10.60	10.56
	Q_{CL}	36,500	35,000
NW	d (nm)	28	25
	l (µm)	24	12

The mechanical properties of the Si cantilevers (spring constants k_{CL}, effective masses m_{CL}, eigenfrequencies ω_{CL}, and quality factors Q_{CL}) and the Si NWs (diameter d and length l) used for the coupled devices #1 and #2 are given.

corresponding curve fitting is based on ref. [35]

$$\mathrm{PSD}(\omega) = \frac{A}{\left(1 - (\omega/\omega_a)^2\right)^2 + (\omega/(\omega_a Q_a))^2} + \frac{B}{\left(1 - (\omega/\omega_b)^2\right)^2 + (\omega/(\omega_b Q_b))^2} \quad (1)$$

where A and B are constants.

Figure 1c presents the fitting of the *V*-dependent PSD of device #1. The electrostatic interaction imposed by the bias voltage V leads to a frequency increase which is in contrast to the usual frequency reduction caused by electrostatic attraction in typical cantilever-type SPM settings[36]. The voltage dependency of the coupled modes is mainly governed by the electrostatic interaction at the NW (see Supplementary Note 3).

Electrostatic interaction on the coupled devices. We model the electrostatic interaction acting on the NW end as a spring-like contribution $k_{bias} = rV^2$ where r is an electrostatic constant. For simplicity, we assume the electrostatic system is polarity independent and ignore contact potential differences (CPD) and further effects of asymmetries in the electrostatic system (see

Supplementary Note 4). Note that we also neglect a bias dependency of r which might be caused by a V dependent static NW deflection (see Supplementary Note 3).

Neglecting damping and assuming simple one-dimensional spring-mass systems, the resonance frequencies of the coupled modes $\omega_{a,b}$ read[26,37]

$$\omega_{a,b}^2 = \frac{\omega_{CL*}^2 + \omega_{NW*}^2}{2} \mp \sqrt{\left(\frac{\omega_{CL*}^2 - \omega_{NW*}^2}{2}\right)^2 + \frac{k_{NW}^2}{m_{CL} m_{NW}}} \quad (2)$$

where $\omega_{CL*}^2 = (k_{CL} + k_{NW})/m_{CL}$ and $\omega_{NW*}^2 = (k_{NW} + k_{bias})/m_{NW}$. Even if ω_{CL*} and ω_{NW*} intersect at a particular voltage (gray dashed lines in Fig. 2a), ω_a and ω_b show clear signatures of avoided level crossing or anticrossing[37] as demonstrated in Fig. 1c and Fig. 2a for device #1. A minimal frequency gap $(\omega_b^2 - \omega_a^2)_{min}$ is expected for $\omega_{CL*}^2 = \omega_{NW*}^2$.

The measured frequency data presented in Fig. 2a allow for a precise curve fitting using Eq. 2. The sets of parameters that best fit our measurements include k_{NW}, $\omega_{CL}/2\pi$, $\omega_{NW}/2\pi$ (see Table 2), and r. When considering k_{bias} acting on the NW we may also expect a *V*-dependent effective reduction of the cantilever's spring constant caused by the electrostatic attraction. However, this effect turns out to be negligible in our case (see Supplementary Note 3).

Figure 2b shows the $\omega_b(k_{bias})$ relation. For small increments $\triangle k_{bias}$ of the interaction force derivative where $|\triangle k_{bias}| \ll k_{NW} + k_{bias}$, we can assume a linear approximation for the corresponding shift in the frequency $\triangle \omega_b$, which can be written by $\triangle \omega_b / \omega_b \approx \triangle k_{bias} / 2 k_b^{eff}$. Since k_b^{eff} describes the $\triangle \omega_b(\triangle k_{bias})$ relation, it can be considered as an effective spring constant of the coupled system. Furthermore, k_b^{eff} can be approximated by $2k_{NW}$ if the following requirements are fulfilled: (i) the cantilever spring constant is much larger than that of the NW, $k_{CL}/k_{NW} \gg 1$, and (ii) if the electrostatic interaction is tuned such that the system is driven to the minimum frequency gap $(\omega_b^2 - \omega_a^2)_{min}$ in the anticrossing region[38]. Our measured data
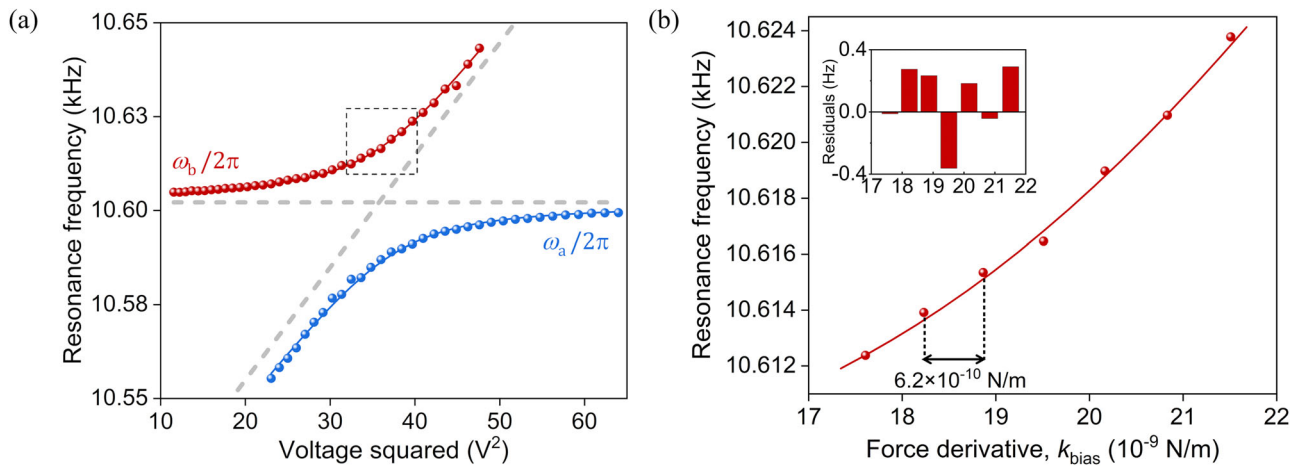
Fig. 2 Frequencies of coupled modes. The measurements of device #1 are shown where spheres and solid lines refer to measurements and fitted curves, respectively. **a** Avoided level crossing of ω_a (shown in blue) and ω_b (shown in red) controlled by the bias voltage V. The cantilever frequency and the nanowire (NW) frequency $\omega_{NW^*}^2 = (k_{NW} + k_{bias})/m_{NW}$ are indicated by gray dashed lines. **b** Magnified view of the section indicated by the dashed rectangle in **a**. The horizontal axis, i.e., the V-induced interaction, is represented as $k_{bias} = rV^2$. Here, $r = 5.4 \times 10^{-10}$ Nm^{-1}V^{-2} as extracted from curve fitting. In the inset, ω_b residuals are shown.

Table 2 Properties of individual and coupled oscillators.

Device #1 Device #2	k_i (N/m)	$\omega_i/2\pi$ (kHz)	Q_i	F'_{min} (N/m) (calculated)	$F' = \Delta k_{bias}$ (N/m) (measured)	k_{CL}/k_{NW}
Cantilever ($i =$ CL)	0.126 ± 0.004 0.140 ± 0.004	10.60 10.56	36,500 35,000	5.1×10^{-6} 5.8×10^{-6}	- -	- -
NW ($i =$ NW)	$(9 \pm 1) \times 10^{-7}$ $(5 \pm 0.5) \times 10^{-6}$	10.495 10.486	675 500	2.8×10^{-10} 1.8×10^{-9}	- -	- -
Coupled system§ ($i = a/b$)	$(1.9 \pm 0.1) \times 10^{-6}$ $(1.07 \pm 0.1) \times 10^{-5}$	10.589/10.616 10.525/10.590	1360 940	4.1×10^{-10} 2.7×10^{-9}	$(9.0 \pm 0.2) \times 10^{-10}$ $(9.8 \pm 0.2) \times 10^{-9}$	1.4×10^5 2.8×10^4

Summary of force constants k_i, resonant frequencies ω_i, quality factors Q_i, minimal detectable force derivatives F'_{min}, measured force derivative uncertainty Δk_{bias}, and force constant ratios k_{CL}/k_{NW} is given for devices #1 and #2. The force derivatives are provided for a measurement bandwidth of 1 Hz at a temperature of 293 K. The electrostatic constant r for device #1 and device #2 is 5.4×10^{-10} Nm^{-1}V^{-2} and 2.0×10^{-9} Nm^{-1}V^{-2}, respectively.
§At bias voltage $V = -6$ V for device #1 and $V = +6$ V for device #2.

confirm this simple $k_b^{eff} \approx 2k_{NW}$ relation which can also be applied to k_a^{eff} for the first coupled mode. Note that $k_{CL}/k_{NW} \approx 140,000$ for device #1 (Table 2).

Minimal detectable force derivative. Our measurements demonstrate that a Δk_{bias} increment as small as $\approx 6 \times 10^{-10}$ N/m leads to a clearly detectable frequency shift $\Delta \omega_b \approx 1.5$ Hz (Fig. 2b). The standard deviation of the ω_b residuals (inset of Fig. 2b) is ≈ 0.3 Hz corresponding to a Δk_{bias} measurement uncertainty of $\approx 1.1 \times 10^{-10}$ N/m. Converted to a measurement scheme at a measurement bandwidth of 1 Hz (see Supplementary Note 5), the Δk_{bias} measurement uncertainty for device #1 would be $\approx 9 \times 10^{-10}$ N/m.

We compare the measured force derivative uncertainty Δk_{bias} to the minimal detectable force derivative F'_{min} as limited by thermal force fluctuations[39,40] at room temperature. F'_{min} is given by

$$F'_{min} = \sqrt{4k_i k_B TB/(\omega_i Q_i (\Delta z)^2)} \qquad (3)$$

Here, Δz is the sensor's root-mean-square vibration amplitude. In our case, the thermal motion variance of the device, i.e., $\Delta z = \sqrt{k_B T/k_i}$ is used according to the equipartition theorem. Note that such calculated F'_{min} considers thermal limitations only and disregards various other noise contributions including detector noise. Therefore, it constitutes a theoretical lower limit that probably cannot be achieved experimentally.

Using Eq. 3, F'_{min} is calculated for the coupled devices, the isolated NWs, and the cantilevers (Table 2). We note that in the case of co-resonance, i.e., $\omega_{CL^*}^2 = \omega_{NW^*}^2$, the minimal detectable force derivative F'_{min} of the coupled devices is of the same order of magnitude as the corresponding quantity of the isolated NWs. In the case of device #1 the calculated $F'_{min} = 4.1 \times 10^{-10}$ N/m is only 45 % larger than that of the isolated NW, but at the same time, it is four orders of magnitude smaller than that of the corresponding standalone cantilever. Furthermore, the $F' = \Delta k_{bias}$ measurement uncertainty is approximately 2.2 times larger than F'_{min} for device #1 yet still roughly four orders of magnitude smaller than F'_{min} of the corresponding standalone cantilever. These findings are additionally confirmed by the analysis of device #2 (Table 2, Fig. 3, and Supplementary Note 7).

In Fig. 3, F'_{min} is shown for the coupled devices, for the corresponding standalone cantilevers and Si NWs together with the measured force derivative uncertainty Δk_{bias} and F'_{min} values derived from literature[11,15,20,34,41–46]. The data is arranged according to the respective typical widths of the sensors at a particular location where usually optical detection is performed. Therefore, a larger "typical width" is associated with easier detection of the signal (depicted by the arrow). Optical detection of our coupled systems is done at the cantilever near its free end where the NW is attached.

Note that the data points describing the devices and device components of this work are grouped in three clusters. If
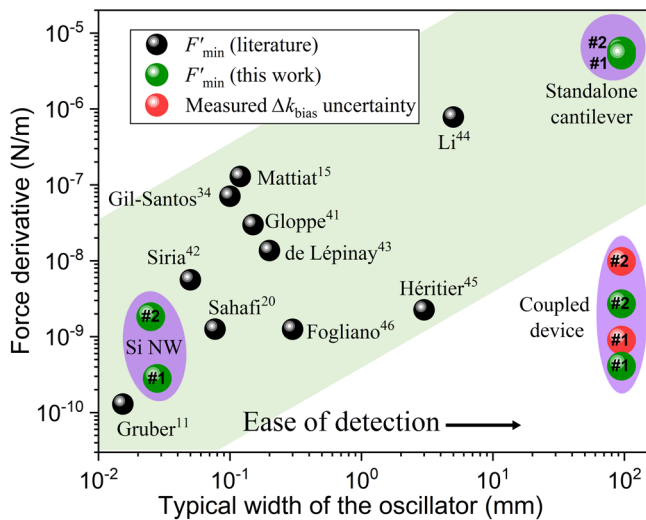
Fig. 3 Minimal detectable force derivative. The F'_{min} is shown as limited by thermal force fluctuations at a measurement bandwidth of $B = 1$Hz and at room temperature versus the typical width of the oscillator devices. Typical oscillator widths refer to the dimension of the optically detected sensor part, i.e., the diameter of the nanowire (NW) in the case of standalone NWs and the width of the cantilever in the case of standalone cantilevers and coupled devices. Calculated F'_{min} is given for the coupled devices, the standalone cantilevers and Si NWs of devices #1 and #2, and for singly-clamped NW and cantilever devices as reported in literature[11,15,20,34,41–46]. In addition, the measured force derivative uncertainty $\triangle k_{bias}$ of our coupled devices is shown. The light-green background indicates the expected trend for nano- and micro-scale cantilevers.

considered as standalone devices, the Si NWs are associated with high force derivative sensitivity but challenging direct detection (bottom left purple ellipse in Fig. 3). At the same time, the micron-sized cantilevers are associated with lower force derivative sensitivity but easy detectability (top right purple circle in Fig. 3). Our co-resonantly coupled devices (bottom right purple ellipse in Fig. 3) advantageously combine the NWs' high sensitivity with the cantilevers' easy detectability.

Now, we discuss the characteristics of the minimal detectable force derivative F'_{min} as limited by thermal force fluctuations (Eq. 3) when comparing a standalone NW to the same NW when co-resonantly coupled to a micro-cantilever. The doubled effective force constant, i.e., $k_{a/b}^{eff} \approx 2k_{NW}$, deteriorates F'_{min} by a factor of $\sqrt{2}$, but at the same time, there is the advantage of increased quality factor, i.e., $Q_{a/b}^{eff} > Q_{NW}$. The latter can be considered as the lending of the cantilever's high quality factor to the co-resonantly coupled modes[38]. This effect has also been described for micron-sized drum resonators coupled to Si_3N_4 membranes[47]. For perfect frequency matching $\omega_{CL^*}^2 \approx \omega_{NW^*}^2$ and very different individual quality factors $Q_{CL} \gg Q_{NW}$ like in our case, the effective quality factors $Q_{a/b}^{eff}$ are approximately doubled, i.e., $Q_{a/b}^{eff} \approx 2Q_{NW}$ (see Supplementary Note 6). Thus, the k_i/Q_i ratio in Eq. 3 does not change upon co-resonant coupling of a NW. The moderate F'_{min} increase as apparent in Table 2 is caused by the decrease of the thermal motion variance upon coupling. In other words, F'_{min} would not deteriorate upon coupling if the systems were driven at constant $\triangle z$.

Similar to Fig. 3, a compilation and comparison of force derivatives could also be done by considering vibration amplitudes $\triangle z$ driven by periodic excitations that exploit the full dynamic range[48] of the respective oscillators. However, the latter might only be appropriate where large oscillation amplitudes are compatible with the specific sensor application, e.g., in mass sensing[17].

In order to understand the dependency of F'_{min} on the device dimensions we can divide $F_{min} \propto d/\sqrt{l}$ by the thermal motion variance, i.e., $\triangle z \propto \sqrt{1/k_i} \propto l^{3/2}/d^2$ resulting in $F'_{min} \propto d^3/l^2$. Thus, devices comprising long and thin NWs will be the most sensitive. If we want to simultaneously maximize the frequencies and minimize F'_{min}, all NW dimensions should be scaled down[13]. Here we specifically point to NW dimensions since F'_{min} of coupled devices is mainly defined by NW properties.

Possible mechanisms underlying the bias-induced NW frequency increase include a softening effect caused by the derivative of the attractive electrostatic force leading to a negative frequency shift, a pendulum-type effect that is expected for a NW tilted towards the counter electrode and exposed to an attractive force leading to a positive frequency shift, and an effective stiffening by bias-induced static NW bending taking into account geometrical nonlinearities. We calculated the sum of these contributions for device #1 at −6V. However, it accounts only for 10% of our experimentally obtained $k_{bias} = rV^2$ (see Supplementary Note 3). To provide a full analysis of the mechanism behind the voltage-dependent NW stiffening further studies are required.

Conclusions

Our results demonstrate that co-resonantly coupled NW-cantilever systems, i.e., systems with matched individual eigen-frequencies $\omega_{CL^*}^2 \approx \omega_{NW^*}^2$, can detect small force derivatives of a similar order of magnitude to those of standalone NWs (Fig. 3). The coupled, hybrid modes of a NW-cantilever system reflect the vibration properties of the involved NW even if the coupled system is several orders of magnitude larger than the NW. At the same time, the coupled system can be read out by conventional cantilever detection methods that are widely used in commercial SPM setups.

The detection sensitivity of force and force derivative sensors based on coupled oscillators can be further improved by: (i) direct growth of NWs on cantilevers which will increase the NWs' Q factors by several orders of magnitude[20] and (ii) miniaturization of the coupled device, e.g., coupling a $k = 10^{-9}$N/m single-walled carbon nanotube to an interferometrically detected $k = 10^{-4}$N/m NW or soft cantilever.

A potential advantage of coupled NW-cantilever devices might be that they allow for sensing at much lower NW temperatures compared to optically detected NW-only sensors since the NWs of coupled devices are not exposed to optical heating.

There is a variety of possible implementations of the co-resonantly coupled sensor. A feasible mode of operation can be that the electrostatic interaction at the NW end is controlled by a feedback loop which keeps the frequencies of the coupled modes constant, preferably in the frequency-matching region $\omega_{CL^*}^2 = \omega_{NW^*}^2$. This would keep the overall interaction at the NW end constant and would ensure that the electrostatic interaction associated with the voltage would reflect changes in the external interaction.

The prospect for future applications of co-resonantly coupled NW-cantilever systems may include nano-torque magnetometry[18] of single endohedral fullerene molecules or corresponding nano-crystallites[49], sensing of ultra-small masses, and scanning probe microscopy approaches[15,42,50]. For the latter, the NW part of the sensor should be arranged in the pendulum geometry to avoid snap-in. Additionally, a straight NW shape would be necessary to ensure an adequate longitudinal NW stiffness.

Methods

Fabrication of coupled oscillator devices. We used As-doped Si NWs (diameters d: 15 nm to 30 nm; lengths l: 10 μm to 30 μm) grown by catalytic epitaxial chemical vapor deposition (CVD) using an Applied Materials P5000 cluster tool. The growth was carried out at a temperature of 450 °C and a pressure of 67 mbar. Details of the NW growth are described elsewhere[51]. The coupled oscillators were prepared using a micromanipulation device (Kleindiek micromanipulator) inside a combined scanning electron microscopy (SEM) and focused ion beam (FIB) instrument (ZEISS 1540 XB) equipped with a gas injection system. The NWs were glued to tip-less Si cantilevers (NanoWorld Arrow TL; triangular apex removed by FIB milling) by electron-beam-assisted deposition of tungsten (Fig. 1a, b).

Data availability

The data analyzed and presented in this study are available from the corresponding author upon reasonable request.

References

1. Jia, C., Lin, Z., Huang, Y. & Duan, X. Nanowire electronics: from nanoscale to macroscale. *Chem. Rev.* **119**, 9074–9135 (2019).
2. Patolsky, F. & Lieber, C. M. Nanowire nanosensors. *Mater. Today* **8**, 20–28 (2005).
3. Im, J. H. et al. Nanowire perovskite solar cell. *Nano Lett.* **15**, 2120–2126 (2015).
4. Pondman, K. M. et al. Magnetic drug delivery with FePd nanowires. *J. Magn. Magn. Mater.* **380**, 299–306 (2015).
5. Huang, G. W., Xiao, H. M. & Fu, S. Y. Wearable electronics of silver-nanowire/poly(dimethylsiloxane) nanocomposite for smart clothing. *Sci. Rep.* **5**, 13971 (2015).
6. Yang, Z. et al. Wearable electronics for heating and sensing based on a multifunctional PET/silver nanowire/PDMS yarn. *Nanoscale* **12**, 16562–16569 (2020).
7. Kim, D. et al. A transparent and flexible capacitive-force touch pad from high-aspect-ratio copper nanowires with enhanced oxidation resistance for applications in wearable electronics. *Small Methods* **2**, 1800077 (2018).
8. Yuan, J. et al. Superwetting nanowire membranes for selective absorption. *Nat. Nanotechnol.* **3**, 332–336 (2008).
9. Walke, P. et al. Silver nanowires for highly reproducible cantilever based AFM-TERS microscopy: Towards a universal TERS probe. *Nanoscale* **10**, 7556–7565 (2018).
10. Chiu, H. Y., Hung, P., Postma, H. W. C. & Bockrath, M. Atomic-scale mass sensing using carbon nanotube resonators. *Nano Lett.* **8**, 4342–4346 (2008).
11. Gruber, G. et al. Mass sensing for the advanced fabrication of nanomechanical resonators. *Nano Lett.* **19**, 6987–6992 (2019).
12. Rossi, N., Gross, B., Dirnberger, F., Bougeard, D. & Poggio, M. Magnetic force sensing using a self-assembled nanowire. *Nano Lett.* **19**, 930–936 (2019).
13. Braakman, F. R. & Poggio, M. Force sensing with nanowire cantilevers. *Nanotechnology* **30**, 332001 (2019).
14. da Silva, A. M. et al. Nanowire arrays as force sensors with super-resolved localization position detection: application to optical measurement of bacterial adhesion forces. *Small Methods* **2**, 1700411 (2018).
15. Mattiat, H. et al. Nanowire magnetic force sensors fabricated by focused-electron-beam-induced deposition. *Phys. Rev. Appl.* **13**, 044043 (2020).
16. Freitag, N. H. et al. Simultaneous magnetic field and field gradient mapping of hexagonal MnNiGa by quantitative magnetic force microscopy. *Commun. Phys.* **6**, 11 (2023).
17. Molina, J. et al. High dynamic range nanowire resonators. *Nano Lett.* **21**, 6617–6624 (2021).
18. Stipe, B. C., Mamin, H. J., Stowe, T. D., Kenny, T. W. & Rugar, D. Magnetic dissipation and fluctuations in individual nanomagnets measured by ultrasensitive cantilever magnetometry. *Phys. Rev. Lett.* **86**, 2874–2877 (2001).
19. Banerjee, P. et al. Magnetization reversal in an individual 25 nm iron-filled carbon nanotube. *Appl. Phys. Lett.* **96**, 252505 (2010).
20. Sahafi, P. et al. Ultralow dissipation patterned silicon nanowire arrays for scanning probe microscopy. *Nano Lett.* **20**, 218–223 (2020).
21. Tavernarakis, A. et al. Optomechanics with a hybrid carbon nanotube resonator. *Nat. Commun.* **9**, 662 (2018).
22. Tsioutsios, I., Tavernarakis, A., Osmond, J., Verlot, P. & Bachtold, A. Real-time measurement of nanotube resonator fluctuations in an electron microscope. *Nano Lett.* **17**, 1748–1755 (2017).
23. Purcell, S. T., Vincent, P., Journet, C. & Binh, V. T. Tuning of nanotube mechanical resonances by electric field pulling. *Phys. Rev. Lett.* **89**, 276103 (2002).
24. Descombin, A. et al. Giant, voltage tuned, quality factors of single wall carbon nanotubes and graphene at room temperature. *Nano Lett.* **19**, 1534–1538 (2019).
25. Perisanu, S. et al. Mechanical properties of SiC nanowires determined by scanning electron and field emission microscopies. *Phys. Rev. B Condens. Matter Mater. Phys.* **77**, 165434 (2008).
26. Reiche, C. F., Körner, J., Büchner, B. & Mühl, T. Introduction of a co-resonant detection concept for mechanical oscillation-based sensors. *Nanotechnology* **26**, 335501 (2015).
27. Körner, J., Reiche, C. F., Büchner, B., Mühl, T. & Gerlach, G. Employing electro-mechanical analogies for co-resonantly coupled cantilever sensors. *J. Sens. Sens. Syst.* **5**, 245–259 (2016).
28. Körner, J. et al. Magnetic properties of individual Co_2FeGa Heusler nanoparticles studied at room temperature by a highly sensitive co-resonant cantilever sensor. *Sci. Rep.* **7**, 8881 (2017).
29. Körner, J. et al. Signal enhancement in cantilever magnetometry based on a co-resonantly coupled sensor. *Beilstein J. Nanotechnol.* **7**, 1033–1043 (2016).
30. Li, X., Ono, T., Lin, R. & Esashi, M. Resonance enhancement of micromachined resonators with strong mechanical-coupling between two degrees of freedom. *Microelectron. Eng.* **65**, 1–12 (2002).
31. Akiyama, T., Staufer, U., De Rooij, N. F., Frederix, P. & Engel, A. Symmetrically arranged quartz tuning fork with soft cantilever for intermittent contact mode atomic force microscopy. *Rev. Sci. Instrum.* **74**, 112–117 (2003).
32. Vidal-Álvarez, G. et al. Top-down silicon microcantilever with coupled bottom-up silicon nanowire for enhanced mass resolution. *Nanotechnology* **26**, 145502 (2015).
33. Nelis, M. R. et al. Sources and implications of resonant mode splitting in silicon nanowire devices. *Nanotechnology* **22**, 455502 (2011).
34. Gil-Santos, E. et al. Nanomechanical mass sensing and stiffness spectrometry based on two-dimensional vibrations of resonant nanowires. *Nat. Nanotechnol.* **5**, 641–645 (2010).
35. Lübbe, J. et al. Thermal noise limit for ultra-high vacuum noncontact atomic force microscopy. *Beilstein J. Nanotechnol.* **4**, 32–44 (2013).
36. Melitz, W., Shen, J., Kummel, A. C. & Lee, S. Kelvin probe force microscopy and its application. *Surf. Sci. Rep.* **66**, 1–27 (2011).
37. Novotny, L. Strong coupling, energy splitting, and level crossings: A classical perspective. *Am. J. Phys.* **78**, 1199–1202 (2010).
38. Körner, J. Effective sensor properties and sensitivity considerations of a dynamic co-resonantly coupled cantilever sensor. *Beilstein J. Nanotechnol.* **9**, 2546–2560 (2018).
39. Dürig, U., Gimzewski, J. K., Pohl, D. W. & Schlittler, R. Force sensing in scanning tunneling microscopy. *IBM Res. Rep.* No. RZ1513 (1986).
40. Albrecht, T. R., Grütter, P., Horne, D. & Rugar, D. Frequency modulation detection using high-Q cantilevers for enhanced force microscope sensitivity. *J. Appl. Phys.* **69**, 668–673 (1991).
41. Gloppe, A. et al. Bidimensional nano-optomechanics and topological backaction in a non-conservative radiation force field. *Nat. Nanotechnol.* **9**, 920–926 (2014).
42. Siria, A. & Niguès, A. Electron beam detection of a nanotube scanning force microscope. *Sci. Rep.* **7**, 11595 (2017).
43. De Lépinay, L. M. et al. A universal and ultrasensitive vectorial nanomechanical sensor for imaging 2D force fields. *Nat. Nanotechnol.* **12**, 156–162 (2017).
44. Li, M., Tang, H. X. & Roukes, M. L. Ultra-sensitive NEMS-based cantilevers for sensing, scanned probe and very high-frequency applications. *Nat. Nanotechnol.* **2**, 114–120 (2007).
45. Héritier, M. et al. Nanoladder cantilevers made from diamond and silicon. *Nano Lett.* **18**, 1814–1818 (2018).
46. Fogliano, F. et al. Ultrasensitive nano-optomechanical force sensor operated at dilution temperatures. *Nat. Commun.* **12**, 4124 (2021).
47. Jaeger, D. et al. Mechanical mode imaging of a High-Q hybrid hBN/Si_3N_4 resonator. *Nano Lett.* **23**, 2016–2022 (2023).
48. Ekinci, K. L. & Roukes, M. L. Nanoelectromechanical systems. *Rev. Sci. Instrum.* **76**, 061101 (2005).
49. Liu, F. et al. Single molecule magnet with an unpaired electron trapped between two lanthanide ions inside a fullerene. *Nat. Commun.* **8**, 16098 (2017).
50. Reiche, C. F., Körner, J., Büchner, B. & Mühl, T. Bidirectional scanning force microscopy probes with co-resonant sensitivity enhancement. *IEEE-NANO 2015—15th Int. Conf. Nanotechnol.* 1222–1225 (IEEE, 2015).

51. Weber, W. M. et al. Silicon nanowires: catalytic growth and electrical characterization. *Phys. Status Solidi Basic Res.* **243**, 3340–3345 (2006).

Author contributions

M.S.: conceptualization, methodology, validation, formal analysis, investigation, data curation, writing—original draft, writing—review & editing, visualization; A.S.P.: software, formal analysis, data curation, writing—review & editing, visualization; N.H.F.: methodology, writing—review & editing, visualization; B.B.: writing—review & editing, supervision, project administration, funding acquisition; T.M.: conceptualization, methodology, formal analysis, resources, writing—original draft, writing—review & editing, visualization, supervision, project administration, funding acquisition.

Competing interests

The authors declare no competing interests.

Additional information

Supplementary information The online version contains supplementary material available at https://doi.org/10.1038/s42005-023-01466-9.

Correspondence and requests for materials should be addressed to Maneesha Sharma or Thomas Mühl.

Peer review information *Communications Physics* thanks the anonymous reviewers for their contribution to the peer review of this work. A peer review file is available.

Reprints and permission information is available at http://www.nature.com/reprints

Publisher's note Springer Nature remains neutral with regard to jurisdictional claims in published maps and institutional affiliations.